Evaluation of dynamic sky-type using novel angular sky luminance measurement system

Marshal Maskarenj, Gaurav Chawla, Rangan Banerjee, Prakash C Ghosh*

Department of Energy Science and Engineering, Indian Institute of Technology Bombay, Powai, Mumbai, 400076, India, e-mail: pcghosh@iitb.ac.in

Abstract

An energy efficient building design needs minimum electric lighting to complement available daylight, while maintaining a defined illuminance value indoors. Design optimization thus needs a good knowledge of dynamic angular sky-luminance distribution, through measurement or models, for simulating indoor illuminance conditions and assessing design performance. Most simulation packages use standard sky-types of the established Commission International de l'Eclairage (CIE) sky-models for generating sky-luminance distribution datasets, which are used for predicting indoor illuminance distribution. However, the sky-type can vary on diurnal and seasonal basis; and there is a need for identifying closest sky-type at different time-points for better indoor illuminance predictions.

This paper aims at measuring angular sky-luminance distribution, and recommending the closest sky-model for a given set by comparing measured datasets with established CIE standard skies. A novel design of a sky-luminance measurement device using calibrated LDRs is proposed to measure incident illuminance from 265 discrete patches in the sky-hemisphere every 5 minutes. A statistical analysis is performed on the 540 representative measured datasets across five-month period and the closest CIE sky-type for various hours is recommended based on the occurrence through the day. A range of 9 CIE sky-types was determined as closest-model skies through the captured datasets in Mumbai, and CIE sky-type 8 is identified dominating most hours in the measured datasets.

Keywords: Building daylight modelling; CIE sky model; Angular sky luminance distribution; Temporal sky-type recommendation; Indoor daylight prediction; Sky scanner

Highlights

- Design of improved LDR based angular sky luminance distribution measurement device
- Sky-luminance distribution measured with 5-minute interval across 5-month period
- Statistical analysis for choosing closest CIE sky for each measured dataset
- Recommendations on sky-type occurrence through different hours of a day
- Frequency of occurrence for different CIE skies over 5-month period in Mumbai

NOMENCLATURE

- **α** Azimuth angle of sky patch (degree)
- **α_s** Azimuthal angles of the Sun (degree)
- **a,b,c,d,e** CIE coefficients
- **A_{in}** Analog input data logged at the microcontroller
- **χ** Angular distance between Sun and sky-patch (degree)
- **f_χ/f_{Zs}** Scattering Indicatrix ratio
- **γ** Elevation angle (degree)
- **L_{in}** Iluminance data at the sensor (lux)
- **L_z** Luminance at altitude Z (cd/m^2)
- **L_{Zen}** Luminance at Zenith (cd/m^2)
- **φ_Z/ φ_0** Luminance gradation ratio
- **R_L** LDR Resistance (ohm)
- **Z_s** Solar zenith angle (degree)

ABBREVIATIONS

- **CIE:** *Commission International de l'Eclairage*: International Commission in Daylighting
- **FOV:** Field of View
- **IDMP:** International Daylight Measurement Program
- **LDR:** Light Dependent Resistor
- **RTC:** Real Time Clock
- **RMSD:** Root Mean Squared Deviation
- **SMPS:** Switching Mode Power Supply
- **SSLD:** Standard Sky Luminance Distribution

1. Introduction

Buildings contribute to a significant share of energy end-use globally, and this is set to increase owing to accelerated urbanization in coming years. Buildings account for over 40% of primary energy consumption in the USA and the European Union[1], and 34% in India[2]. Space illumination through artificial lighting further accounts for 14% share in building energy usage in the European Union, 26% in the USA[3], and 28% in India[4,5]. A good way of reducing building energy consumption is through replacing the disconnected cocoon concept — where the building shell is disconnected from the environment, and needs artificial supply of light, ventilation and thermal comfort[6] — with the connected membrane concept, where the building shell is kept in contact with the environment[7]; and recent works have reported energy use simulation and optimization in non-conventional building designs[8,9] towards higher energy efficiency. Indoor daylight optimization provides a potential in environmental integration, affecting two major segments contributing to building energy use: space lighting and space heating/cooling[10], and literature has proposed the use of skylights and light guidance systems[11–14] as additional avenues beside windows towards maximizing daylight use inside built spaces.

To quantify any significant advantage achieved through a design modification or retrofit in terms of energy saving and enhanced visual comfort, there is a need for analyzing the overall performance of the building[15]. Simulating building performance provides multiple options towards design optimization, and thus is more cost efficient in evaluating building performance as compared to metering physical building systems. Beside computational simulations through software packages[16–20], physical scale models have been used for optimizing building designs[21]. An energy efficient building design requires minimum electric lighting for complementing available daylight while maintaining a defined illuminance level indoors — such a design may be considered optimum in terms of indoor lighting. This needs a quantification of indoor illuminance distribution contributed by daylight, through prediction or measurement, and few possible pathways for predicting indoor illuminance are demonstrated in Figure 1.

Three daylight components contribute to the indoor illuminance at any point: Sky Component, Externally Reflected Component and Internally Reflected Component[22] — of which the Sky Component is the actual source. Thus, dynamically assessing luminance of the ambient sky at multiple angular positions is essential for predicting indoor illuminance. The sky-luminance distribution may be measured, or predicted through sky-models. Measuring sky-luminance at different angular positions dynamically is challenging, hence models have been used to generate sky-luminance data at various spatial positions.

The early works on indoor illuminance distribution predictions through Daylight-Factor concept used Lambertian sky model (1760) — where the luminance for all discrete sky-segments was assumed uniform. This was due to the lack of measurement equipment, and also the lack of computational techniques for implementing complex models. After over a century of acceptance of the Lambertian model, it was challenged by the Moon-Spencer model[23], which proposed an altitudinal gradient between the horizon and the zenith. Owing to the complexity in measuring the luminance of the circumsolar region, effect of the solar position wasn't accounted for in these models. Models with no azimuthal variations assumed an overcast sky-type and could be used towards computing Daylight Factor indoors: a metric based on light levels inside a structure to the light levels outside the structure, used in evaluating the merit of a construction towards daylight addition and illuminance performance. An initial approach in incorporating the sun-position was proposed in Kittler's clear sky model in 1967[24] and published as ISO/CIE model in 1996[25]. The clear-sky model was further generalized into the present standard model accepted by *Commission International de l'Eclairage* (CIE) , which is capable of simulating most-probable skies: a set of 15 skies covering five overcast, intermediate and clear skies each. This model incorporates the gradation with scattering phenomena: involving Rayleigh and Mie scattering behaviors[26]. Researchers have built upon the model and validated it further through measurements at different locations[27–32].

In predicting indoor illuminance, validated simulation packages use standard sky-types of the CIE model along with zenith luminance data from weather files, and create a set of modelled skylight distribution data. These packages use generic sky-models (standard overcast sky[33] or standard clear sky model), as demonstrated in pathway 1 of Figure 1; or provide the user an option to choose from few pre-defined sky-models[34]. Model based calculations for sky-luminance distribution is acceptable in absence of measured data, however, this approach with generic sky-models has been demonstrated to underestimate the indoor illuminance as compared to measurement based sky-models[35].

Another approach for predicting indoor illuminance is through using actual sky data — feeding measured angular incident illuminance datasets into models for calculating indoor distribution, as demonstrated in pathway 3 of Figure 1. Literature reports devices[36–38] and methods[39] for measuring sky-luminance at different angular positions, and our previous work[40] proposes a low-cost LDR-based device to dynamically measure the angular discretized sky-luminance. Using such devices, measured data could replace modelled datasets for performing indoor illuminance distribution calculations. However, the magnitude of measured datasets provides a challenge: the measured luminance distribution datasets are arranged as arrays for the patch's altitudinal and azimuthal placement for each time instant. In contrast, existing simulation packages accept weather data files as input — where multiple environmental parameters are tabulated on hourly basis: dry bulb temperature, wind speed, global horizontal radiation, etc[41]. To incorporate the large datasets for each time instance in existing packages poses a challenge, and may require entirely new simulation packages designed to use measured sky-luminance datasets.

Existing simulation packages are advanced, calculating net energy consumption based on other factors besides lighting overload: heating, ventilation, plug-loads, occupant behavior, etc. As such, it is advisable to avoid the need of designing entirely custom simulation packages and propose a possibility to improve the existing simulation packages. A possible approach is by using open source simulation packages like OpenStudio[42,43], and recommend appropriate model for calculating the sky-luminance distribution. Pathway 2 of Figure 1 demonstrates this approach: measured datasets are compared with various modelled values, and through statistical analysis, the closest sky-type is recommended for any given sky-condition.

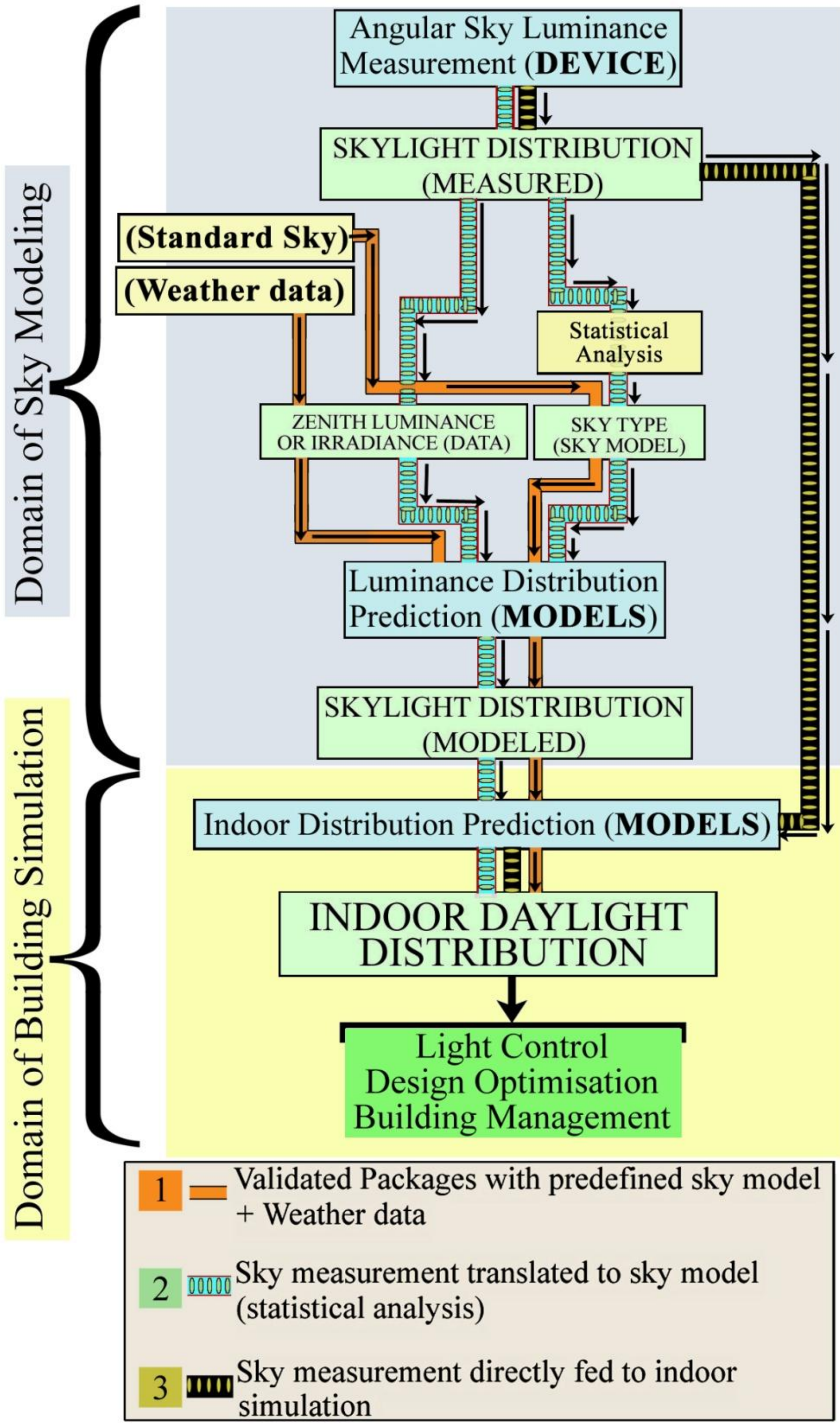

Figure 1: Motivation behind the work: schematics of various approaches towards predicting indoor illuminance distribution. This work covers domain of sky-modelling.

In building simulation, the accuracy of the net output depends on the models employed in a simulation package, and this can be enhanced by using validated models. The CIE standard overcast sky model, one of the 15 most-probable skies in the CIE model is azimuthally independent, and most simulation packages use this model as industry standard[33] for predicting Daylight Factor. The CIE standard clear sky model is optional in few simulation packages. DesignBuilder — a building simulation package[20,44] also offers the users the possibility of choosing from a few intermediate CIE model-skies: sunny clear day, clear day, uniform cloudy day, overcast day, etc[34]. However, there is a variation in the sky-luminance distribution behavior on a diurnal and seasonal basis, and using same sky-model through various times of the year reflects badly in indoor illuminance predictions. Thus, there is a need for identifying the closest CIE sky type for any angular discretised incident illuminance dataset, corresponding to a location and a time of the year. This approach can help create an identifier for the closest CIE sky-model at a given time-instant, which could be used for calculating the sky-luminance distribution in existing simulation programs and thus performing annual energy analysis of building systems.

Literature reports works done in line with evaluating most probable skies at few sites: Hong Kong[26], Singapore[30], and Spain[45] over long scan periods. These works have categorized occurring ambient sky at respective locations using Root Mean Square Deviation (RMSD) approach — the lowest RMSD between theoretical and experimentally measured angular discretised inciden illuminance distribution for a dataset was the identifier for closest sky-type — and thus frequency of occurrence of either of the sky-types over the scan period was analyzed. These works could be extended in terms of identifying the variation in sky-types across time, owing to the dynamic nature of daylight through the day, and due to seasonal and diurnal variations in the sky clarity. These identified closest sky-models could replace generic sky-models in simulation packages, and enhance the reliability of indoor illuminance predictions.

We propose a pathway-2 based approach towards identifying and recommending closest sky-model for any measured data-set, along with a protocol for identifying sky-type as part of annual weather database for a location. The most-probable CIE sky-type is identified for a location over a larger time-period (seasonal) or through various times of the day (diurnal). This is done so the simulation programs can predict indoor illuminance distribution with higher accuracy. Sky luminance studies in literature have reported the use of commercially available daylight scanners (Eko MS 300LR[26,30]/MS 321-LR[45]) for measurement, where the cost of device is a hindrance towards wider reach. In this work, we have used a structurally modified Fresnel-like version of our previously proposed LDR-based low-cost sky-luminance measurement device[40] for measuring sky-luminance every 5-minutes over 5-month period in Mumbai, India. Our low-cost device — developed at about 1/600th the cost of the commercially used sky-scanner[1] — was thus used to measure sky-luminance and collect data to be analyzed into the closest sky-type.

Statistical analysis using RMSE approach was performed on 540 representative measured datasets comprising 265 sky-positions for 4 representative days, and recommendations are given towards frequency of occurrence over the test period. A protocol for identifying the closest sky-type for each dataset is also proposed, and the diurnal variation pattern for closest sky-models is presented. To validate the closest-sky recommendation, a comparison between datasets for measured sky-luminance and modelled closest CIE sky-type is demonstrated. While the RMSE approach taken for identification of closest sky-type is inherently simple, the novelty is in analysis of originally measured data to present diurnal variations between sky-types, which is

[1] EKO MS-321LR quoted at about USD 37,500 including landing charges and taxes in July 2017

presented for few sample days. RMSE based approach for defining Frequency of Occurrence has been used for Hong Kong (2003) [26], Singapore (2007) [30] and recently for Burgos, Spain (2018) [45] using commercial sky-luminance measurement setup, and we have used a low-cost device for analyzing sky-luminance measurements for Mumbai: identifying the Frequency of Occurrence along with Diurnal Variation in sky-types.

2. CIE standard sky model

The CIE standard skies covers a range of most probable skies, with a proposed total of 15 different skies having 5 overcast, 5 intermediate and 5 clear sky types[26,46]. These skies are modifications in the CIE model with different coefficients as tabulated in Table 2 representing various skies depending on the sky type. In general, the CIE sky model describes the luminance ratio between any sky-patch at a given azimuth and altitude with respect to luminance at zenith; as such the measured value of zenith luminance is ample to predict the luminance of all patches of the sky-hemisphere. The luminance ratio for the arbitrary sky element is represented as a combination of gradation ($\varphi_Z/\ \varphi_0$) and indicatrix (f_χ/f_{Zs}) ratios as[24]:

$$\frac{L_{\gamma\alpha}}{L_z} = \frac{f(\chi).\,\varphi(Z)}{f(Z_s).\,\varphi(0^{\circ})} \tag{1}$$

Luminance gradation factor ($\varphi_Z/\ \varphi_0$) accounts for the ratio between the luminance of any sky element to the luminance at zenith at any instance, and comes from the early gradation based models. Scattering indicatrix ratio (f_χ/f_{Zs}) is an addition to the gradation based models — it accounts for the contribution of the sun position — and considers the luminance of a sky element based on its angular distance from the Sun. Here, χ is the angular distance of the patch from sun position, and can be calculated based on the zenith angle of the Sun (Z_s), zenith angle of the sky patch (Z), azimuthal angles of the Sun (α_s) and azimuth of the sky patch (α) respectively, as:

$$\chi = \cos^{-1}(\cos Zs\,.\cos Z + \sin Zs\,.\sin Z\,.\cos(|\alpha - \alpha_s|)) \quad (2)$$

The gradation for a sky element at angle Z from zenith is defined as:

$$\varphi(Z) = 1 + a.\exp\left(\frac{b}{\cos Z}\right) \quad (3)$$

By definition, the value of angle Z at zenith is 0 degrees, as such,

$$\varphi(0°) = 1 + a.\exp(b) \quad (4)$$

Scattering indicatrix factors account for contribution of Sun position as follows:

$$f(\chi) = 1 + c.\left(\exp(d.\chi) - \exp\left(d.\frac{\pi}{2}\right)\right) + e.\cos^2\chi \quad (5)$$

The indicatrix function at the zenith depends on zenith distance of the Sun:

$$f(Z_s) = 1 + c.\left(\exp(d.Z_s) - \exp\left(d.\frac{\pi}{2}\right)\right) + e.\cos^2 Z_s \quad (6)$$

Mie scattering is represented by the ‘dχ’ term: it rapidly reduces at angles farther from the sun exponentially through negative tabulated values for coefficient-‘d’. Rayleigh scattering is incorporated in the e.cos$^2\chi$ term: the effect at 90° angle from the Sun position is zero[26]. The values of Z_s and χ are affected by the instantaneous position of the Sun, and can be calculated through the latitude angle, the day of the year and the time of day. The CIE sky model can be reduced to any of the 15 standard skies[46] by incorporating the values of the coefficients a, b, c, d, and e, tabulated in Table 1.

Table 1: Standard coefficients for most probable sky types

	φ( )	f( )	a	b	c	d	e	Description of Luminance Distribution
1	I	1	4.0	-0.7	0	-1.0	0.00	Overcast, steep luminance gradation towards zenith, uniform azimuthally: **CIE Standard Overcast Sky**
2	I	2	4.0	-0.7	2	-1.5	0.15	Overcast, steep luminance gradation & slight brightening near Sun
3	II	1	1.1	-0.8	0	-1.0	0.00	Overcast, moderately graded and azimuthally uniform
4	II	2	1.1	-0.8	2	-1.5	0.15	Overcast, moderately graded and slight brightening near Sun
5	III	1	0.0	-1.0	0	-1.0	0.00	Sky of Uniform Luminance
6	III	2	0.0	-1.0	2	-1.5	0.15	Partly Cloudy sky, No gradation, slight brightening near Sun
7	III	3	0.0	-1.0	5	-2.5	0.30	Partly Cloudy sky, No gradation, brighter circumsolar region
8	III	4	0.0	-1.0	10	-3.0	0.45	Partly Cloudy sky, No gradation, distinct solar corona
9	IV	2	-1.0	-0.55	2	-1.5	0.15	Partly Cloudy sky, Sun obscured

10	IV	3	-1.0	-0.55	5	-2.5	0.30	Partly Cloudy sky, bright circumsolar region
11	IV	4	-1.0	-0.55	10	-3.0	0.45	White blue sky with distinct solar corona
12	V	4	-1.0	-0.32	10	-3.0	0.45	**CIE Standard Clear Sky,** low illuminance turbidity
13	V	5	-1.0	-0.32	16	-3.0	0.30	**CIE Standard Clear Sky,** polluted atmosphere
14	VI	5	-1.0	-0.15	16	-3.0	0.30	Cloudless turbid sky with broad solar corona
15	VI	6	-1.0	-0.15	24	-2.8	0.15	White-blue turbid sky with broad solar corona

Simulation packages towards indoor illuminance analysis use CIE standard sky-types (overcast and clear)[33] for generating sky-luminance distribution datasets, but actual sky-luminance distribution behavior may significantly differ from the pre-defined sky-type. By comparing sky-luminance measurements for various sky-positions with all probable sky-types, the closest sky-model may be recommended for different time-points over the test period. For this statistical recommendation of closest CIE sky, the actual luminance distribution datasets can be measured using an angular-luminance measurement device.

3. Design of the Angular Luminance Measurement System

A low-cost device with calibrated LDR sensors and open source Arduino Mega 2560 microcontroller is designed and employed for angular incident illuminance measurement and data logging. This device is a modified version of our previous proof-of-concept device[40] which used LDRs and Arduino microcontroller to demonstrate angular sky-luminance measurement. LDRs are chosen as sensing device due to their spectral response matching that of the human eye[47], low noise in the infrared region, low unit cost and high sensitivity to differential light intensity.

3.1 Design Schematics

The device used a microcontroller for capturing sensor data and controlling the azimuthal rotation of the sensing frame. Arduino Mega 2560, a programmable microcontroller was chosen to control the stepper motor and to capture the azimuthal orientation and analog data batch for incident illuminance from each sky-patch position through various timestamps. The LDRs were part of a voltage divider network; variation in incident illuminance changed the LDR resistance causing a potential drop across a fixed resistance, which was measured as the analog data at the microcontroller. For each batch with a 5 minute interval, the azimuthal orientation was captured by a compass sensor, and the timestamp provided by a RTC module. The dataset including the incident illuminance analog data for all sky-patches along with the timestamp and azimuthal orientation data was logged onto a microSD card for further processing. More details about the device fabrication are presented in Sections 3.2 through 3.5.

3.2 Sensor Calibration

LDRs were calibrated for their response to change in incident illuminance from daylight; while LDRs have a good spectral response in the range matching visible light, the calibration was done under natural daylight over a period of 8 hours, extending from pre-noon till dusk of three separate days: 12 May 2017, 9 Jan 2018 and 6 Feb 2018. Two sensors were placed fully exposed facing the zenith and capturing the diffuse horizontal illuminance data, while two were placed facing the zenith with an exposure control matching that of the sensors on the proposed device (11° field of view), the exposure angle being the optimum as proposed by Tregenza[48]. Exposure control here means that the aperture of the sensors is limited to 11º solid angle.

Illuminance (lux) is a product of Luminous intensity (candela) and Solid angle (steradian) normalized per unit area; where Luminous intensity itself is Luminous flux (lm) normalized by the solid angle. The sky-patches are assumed isotropic, hence the factor of the solid angle is neglected; and the units for luminance (cd/m^2) and illuminance (lux) remain same for the assumed isotropic source. Proposed device is used to capture incident illuminance from all sky-patches, including zenith. The ratio between captured incident illuminance values for different patches with respect to that at zenith is analogous to the theoretical luminance ratio ($L_{\gamma\alpha}/L_z$) for modeled sky-luminance distribution used in statistical analysis.

Figure 2 demonstrates the calibration setup. These sensors through a voltage divider network logged their response to varying incident illuminance every two minutes. A commercial digital lux-meter (HTC-LX103) was used to measure the corresponding diffuse illuminance (no exposure control) and also the incident illuminance from zenith (with an 11° field of view tubing) every two minutes.

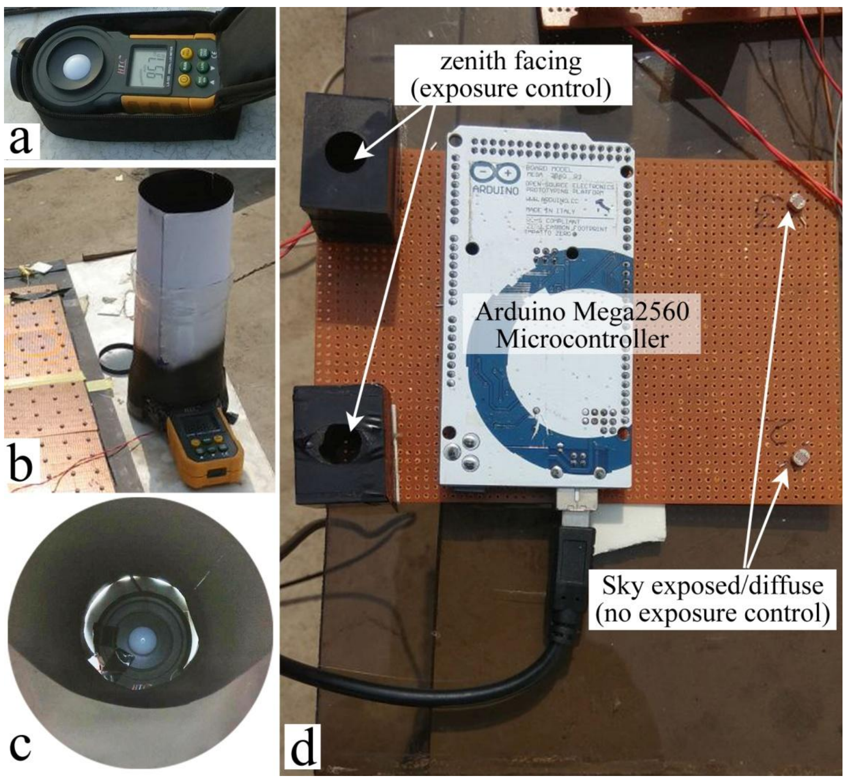

Figure 2: a) Digital lux-meter with no exposure control, b) with a tube to provide 11° FOV for zenith luminance measurement, c) inside the tube view, d) LDR sensors measuring the zenith and diffuse horizontal illuminance and logging data through Arduino microcontroller

Figure 3a demonstrates the calibration curve for the incident illuminance with the captured analog data for the batch of selected LDRs. Since there is a linear correlation of voltage from 0-5V with the analog input from 0-1023, the analog data was converted to corresponding LDR resistance and their logarithmic correlation is demonstrated in Figure 3b. With a very good match between the two (R^2=0.997), the analog input A_{in} could be converted to representative incident illuminance data Lux_{in} with the following correlation:

$$\mathrm{Lux_{in}} = \mathrm{antilog_{10}}\left[7.8553 - 1.6254\,\log_{10}(10{,}000 \text{ x } \left(\frac{1023}{\mathrm{A_{in}}} - 1\right))\right] \quad (6)$$

Figure 3c demonstrates the comparison between measured illuminance and the illuminance value calibrated through analog data.

A linear response is evident for values up to 20,000 lux. Since calibration was performed while maintaining the lux-meter and sensors facing zenith (capturing diffuse horizontal illuminance), most measured values were limited to under 30kLux (~85%), and only the instances with proximity of circumsolar regions close to zenith (12 May 2017) provided values exceeding 40kLux, as tabulated in Table 2.

Table 2: Data points for sensor calibration at different incident illuminance ranges

RANGE OF INCIDENT ILLUMINANCE (KILO LUX)	NUMBER OF DATA-POINTS FOR CALIBRATION	PERCENTAGE
0-10	61	37.4
10-20	53	32.5
20-30	20	12.2
30-40	10	6.1
40-50	15	9.2
50 +	4	2.4

Owing to the low resolution for analog data at higher illuminance values, a large deviation in various discrete measured values with corresponding similar calibrated values is seen for values above 40,000 lux. The error margin for the values plotted in Figure 3c compared with illuminance incident at the measurement device through the day shows acceptable calibration for most of the lower range, with deviation in accuracy for the circumsolar region (~40 klx onwards). Since there were fewer readings in the zone exceeding 50klx, and these sets presented the upper-limit of obtained data; the error margin between calibrated and actual data was seen lesser than the readings around 40klx.

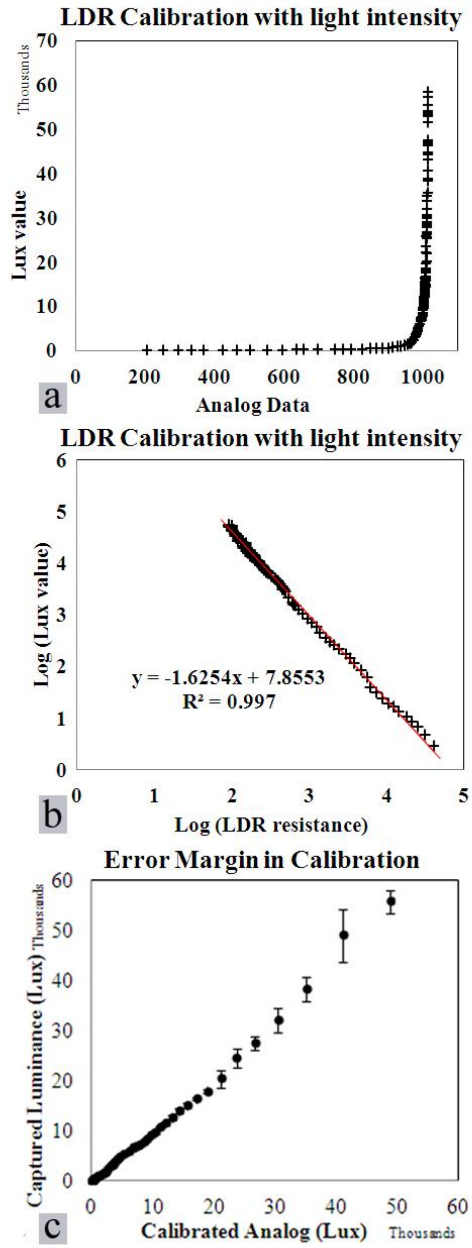

Figure 3: a) Analog data at the microcontroller with corresponding illuminance measured with lux-meter, b) calibration curve for log-plots for LDR resistance and incident patch illuminance, c) error margin in data

3.3 Mechanical Design

The device used in this work is a modification of our previously discussed design[40,49]: the altitudinal orientation of the sensors is done using a Fresnel-like approach to reduce the weight of the device and offer enhanced portability. The rotating frame housing the sensors through exposure control was fabricated using laser-cut acrylic as demonstrated in Figure 4. Through a Fresnel-like configuration, the sensors were specifically oriented at 12 different altitudinal positions: facing Zenith, Z+7.5°, Z+15° and consecutively till Z+82.5°, each measuring a 7.5° altitudinal ring with a 3.75° range on either side of the orientation as demonstrated in Table 3. The term 'discrete range' refers to non-overlapping sections of the sky: as in the ideal case. However, for our 11º exposure with 'exact range' of 5.5º, there was overlap in altitudinal segments. More information has been provided in the Figure 6 and Section 3.5.

Table 3: Sensor Placements in varying altitudinal positions with exposure control

Sensor	Orientation	Discrete range (3.75°)	Exact range (5.5°)
Zenith	Arm 1 (0°)	-3.75° to 3.75°	-5.5° to 5.5°
Zenith + 7.5	Arm 1 (7.5°)	3.75° to 11.25°	2° to 13°
Zenith + 15°	Arm 1 (15°)	11.25° to 18.75°	9.5° to 20.5°
Zenith + 22.5°	Arm 2 (22.5°)	18.75° to 26.25°	17° to 28°
Zenith + 30°	Arm 2 (30°)	26.25° to 33.75°	24.5° to 35.5°
Zenith + 37.5°	Arm 2 (37.5°)	33.75° to 41.25°	32° to 43°
Zenith + 45°	Arm 3 (45°)	41.25° to 48.75°	39.5° to 50.5°
Zenith + 52.5°	Arm 3 (52.5°)	48.75° to 56.25°	47° to 58°
Zenith + 60°	Arm 3 (60°)	56.25° to 63.75°	54.5° to 65.5°
Zenith + 67.5°	Arm 4 (67.5°)	63.75° to 71.25°	62° to 73°
Zenith + 75°	Arm 4 (75°)	71.25° to 78.75°	69.5° to 80.5°
Zenith + 82.5°	Arm 4 (82.5°)	78.75° to 86.25°	77° to 88°

The rotating assembly also housed a compass magnetometer sensor (HMC 5883L) to log the azimuthal orientation of the frame through the rotation for re-orienting the captured data during post processing, if needed. The frame was rotated on a shaft connected to a stepper motor (3.75° per step; 96 steps per revolution) used in dual phase mode, controlled by the microcontroller. With a ~28 second span for completing the azimuthal rotation, the frame was reoriented to initial position every 5 minutes. Figure 4 shows various perspectives of the device.

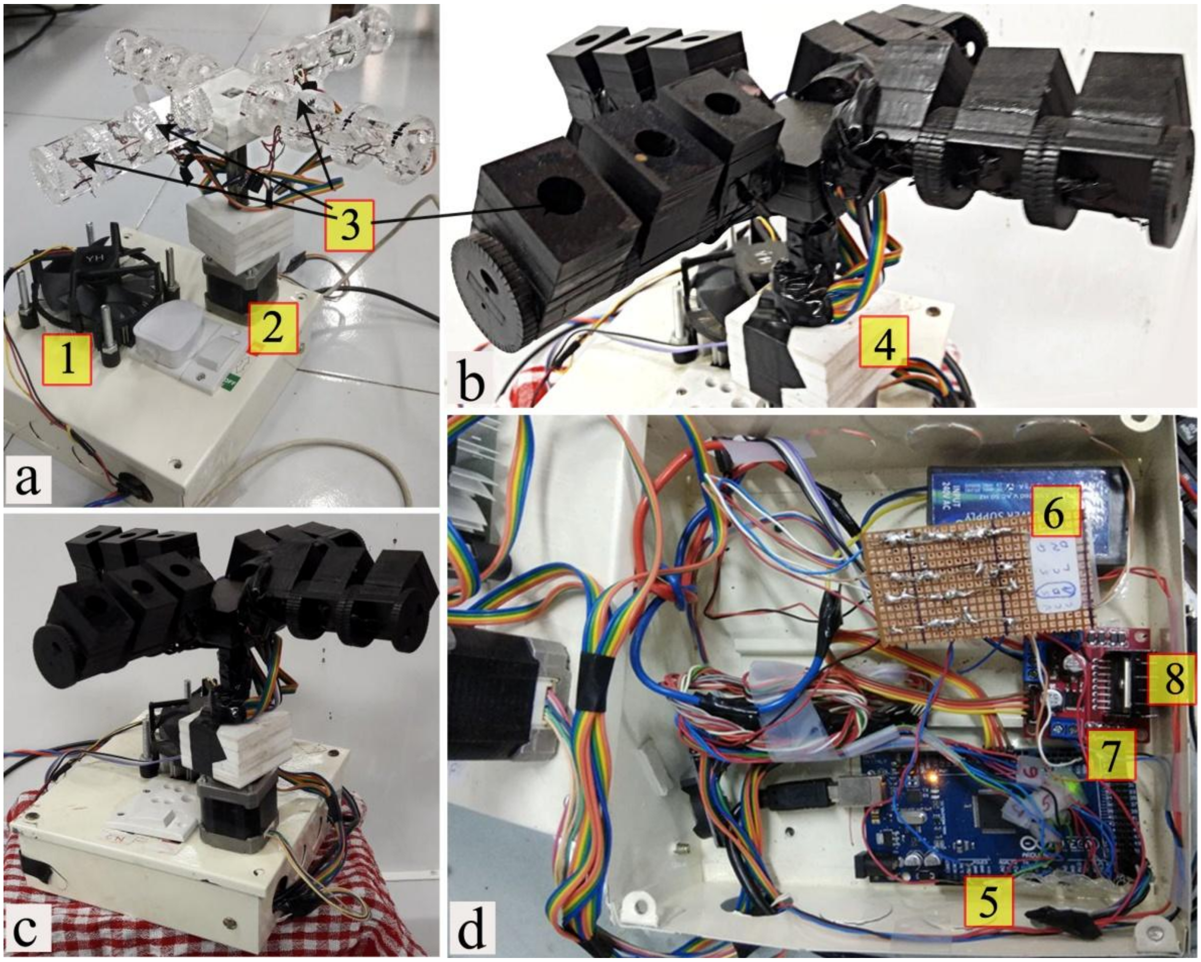

Figure 4: Proposed design, a) rudimentary framework with LDRs placements, b) rotating frame through vertical axis, c) overall device looks, d) under-the hood view.
1) Exhaust cooling fan, 2) Stepper motor, 3) LDR sensors, 4) Rotating shaft, 5) Arduino Mega 2560 microcontroller, 6) 9V SMPS, 7) L298 motor driver, 8) micro SD card shield.

3.4 Data Transposition and logging

Data for each of the 12 sensors was captured at the microcontroller every azimuthal step. However, because of the four arms placed at various azimuthal positions, this data captured at each step of the rotation was transposed before being saved as a batch on the SD card. Figure 5 demonstrates the design of the rotating frame, and the protocol for transposing the data before logging.

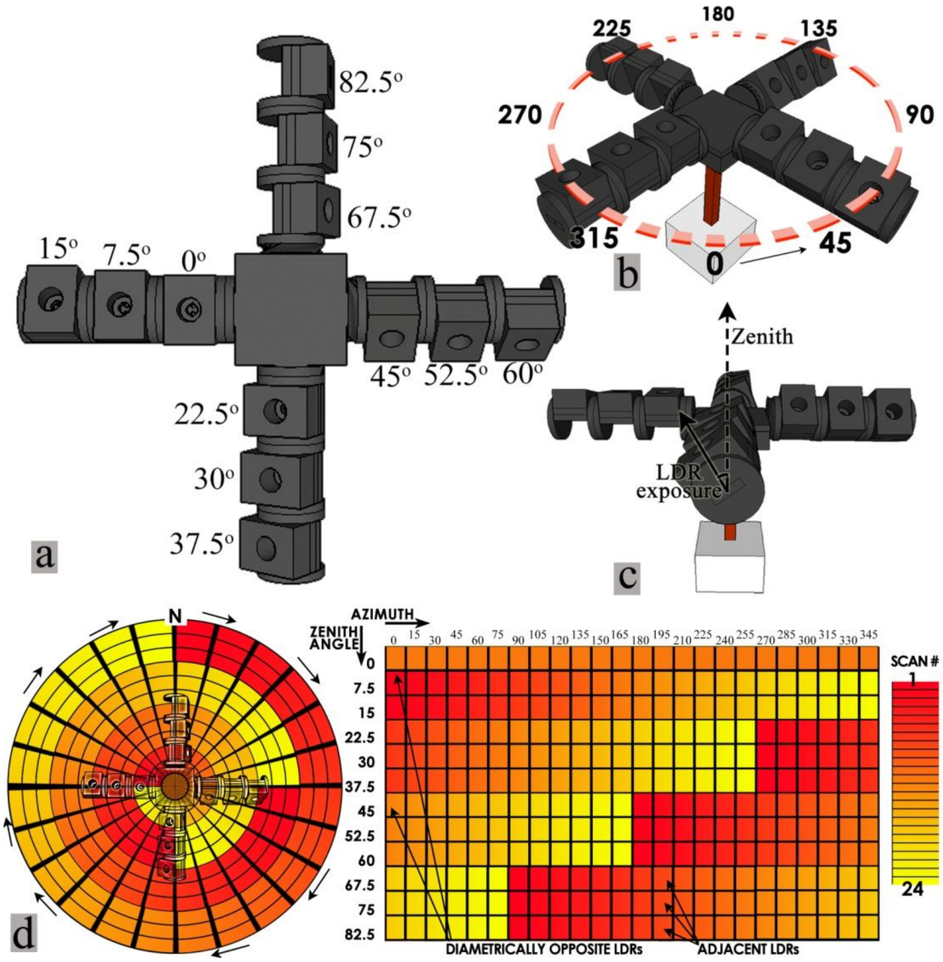

Figure 5: Design of the rotating frame for the device, a) upper view with the sensors facing various altitudinal angles in a Fresnel-like design while on a flat plane, b) various azimuthal positions through 15 degree rotation on a vertical axis, c) side view with visible altitude position for sensors, d) Scan motion and data saving protocol for each LDR from positions 1 through 24.

Through the altitudinal placement and azimuthal rotation of the assembly, the sensors captured incident illuminance data from 265 discrete sky patches: the sky hemisphere was divided into 12 altitudinal rings placed 7.5° apart, each having 24 segments with 15° azimuthal separation, with exposure control to minimize overlaps. The altitudinal placement for the 12 sensors was achieved using a Fresnel-like design, with the exposure controlled sensors facing various orientations while on a planar surface as demonstrated in Figure 5a-c. Azimuthal variations were performed by rotating the assembly on a vertical axis using a stepper motor controlled by the microcontroller, with a compass magnetometer sensor monitoring the precise azimuthal orientation of the assembly. Change in incident illuminance on each sensing LDR produced a change in the LDR resistance, and this resistance change was converted to an analog signal through a voltage divider network that was captured at the microcontroller channel. With an interval of 5 minutes, the analog signal data captured for all sky-patches was logged onto a micro SD card for further processing.

3.5 Comparing sky-subdivision methods: proposed and commercially used

Sky sub-division technique used by commercial scanners discretises the sky-hemisphere into 145 subdivisions (which is a modification of Tregenza's[48] proposed 151 patch subdivision), and is demonstrated Figure 6; along with our proposed sky-scanning protocol into 265 patches (11x24 + zenith).

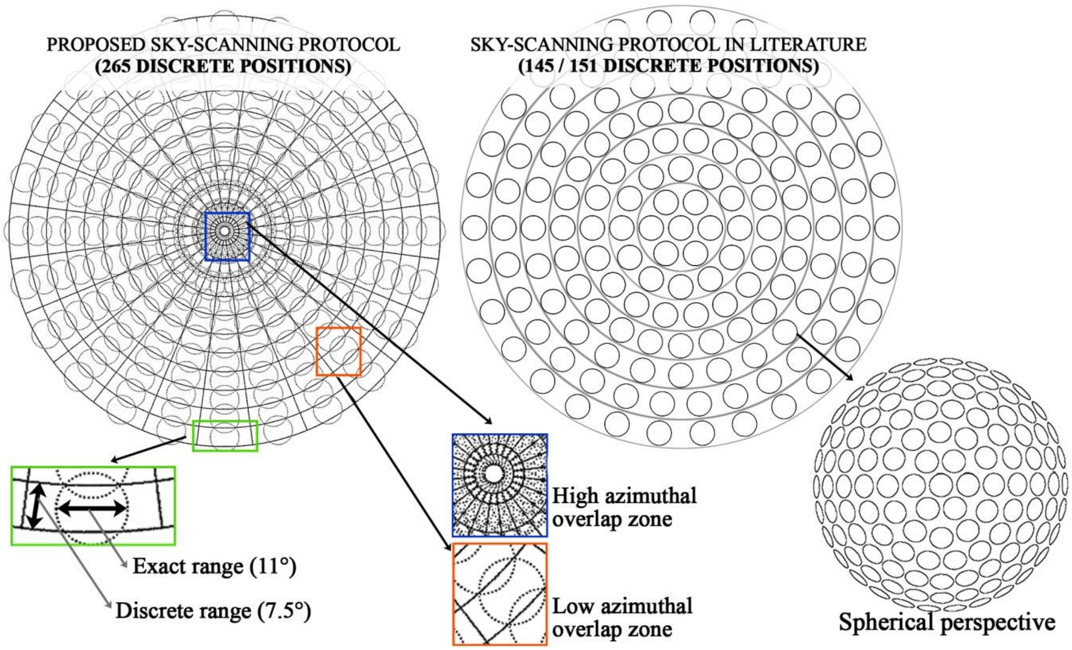

Figure 6: Comparing commercial sky-subdivision technique with the proposed sky-scanning protocol

Tregenza's subdivision discretises the sky-hemisphere into finite equal-sized patches while covering as much of sky as possible; and this covers about 70% of the sky-hemisphere. Our approach was towards simplicity of sky-scanning in vertical axis, and while there is minimal azimuthal overlap in bands from 45 degrees to horizon as seen in Figure 6, the overlap zone between zenith to 45 degrees is significant. To counter the overlap, the captured luminance is normalized by the patch's solid angle to obtain luminance for positions of 1-square degree resolution, which was then interpolated into a cylindrical coordinate for 90x360 degree sky-map.

In indoor calculations, we believe that there is also a need for interpolating data from the 145-subdivision approach too; but owing to overlap at high altitudinal positions, proposed technique measured for more redundant sky-positions.

4. Sky distribution measurement at Mumbai

Mumbai, India is a coastal city located at 19.1°N/72.9°E with 'Aw' climate classified by Köppen-Geiger climate classification[50]. The experimental measurement of sky luminance distribution was conducted on the terrace of Mechanical Engineering department building at Indian Institute of Technology Bombay, located at Powai with an elevation of 50m above mean sea level. Monsoons in Mumbai last between early June and mid October, thus a post-monsoon period was selected for relatively clearer skies. The experimental capture was done on a continuous basis (every 5 minutes) on few days in the months between November 2017 to April 2018, and data was selected based on the compass values: data with compromised rotations were omitted. Few representative days were chosen for analysis: 16 Nov 2017, 30 Jan 2018, 7 March 2018, and 4 April 2018; Days chosen in November and January are almost symmetrically equidistant from the winter solstice, offering similar solar declination angles of S18°35' and S17°53' respectively, and April is an extrapolation of the time-gap (~10 weeks) between the November and January representative days. The week of Jan 30 was generally clearer than the week of Nov 16, and the solar-noon moved closer to zenith in April, as compared to Nov/Jan. The analysis was conducted for days when measurement was logged for the entire duration between dawn to dusk, and sets with incomplete data (owing to device errors like overheating, lack of complete rotation, orientation errors, etc) were not selected. In the secondary selection, representative days from different months were chosen for further analysis. 540 batches of incident illuminance data, with each batch comprising 265 distinct sky-patches at various altitudes and azimuths were considered for further processing and analysis, with net 143,100 distinct analog values separated spatially and temporally being calibrated and analyzed.

5. Data analysis

Each set of captured time-wise data represented 288 analog values for 265 sky patches (24 zenith values averaged to make a composite incident zenith illuminance data) arranged in a 12x24 array defining the altitude and azimuthal positions for each data, which was converted to illuminance data using the calibration equation (Equation 6). The instant discretized angular sky-luminance distribution dataset comprised the incident illuminance value from each patch, including the zenith. To perform a comparison between the measured data with all possible model skies, it is necessary to identify the modelled luminance distribution at these 265 patches for all 15 sky-types. In accordance with Equation 1 through Equation 6, the normalized luminance of each patch ($L_{\gamma\alpha}/L_z$) can be calculated for each model-sky by using representative coefficient values (Table 1) along with two identifiers: the altitude of each sky-patch (α, for gradation factor) and the distance of the patch from the sun-position (χ, for scattering factor). It is important to identify the sun-position at the time instance, to calculate χ and Z_s, and while standard equations are available to predict the sun-position at any time of the year based on the global location[51], our approach was based to address our device limitations.

5.1 Assessment of Sun position from measured data

In our device, the altitude angle was rigidly defined for each sensor position; however, the azimuthal orientation was defined through rotation on a vertical axis. The incident illuminance from various patches was logged for respective azimuthal orientations, which was prone to rotational orientation errors in few cases. To counter this, the sun-position was made independent of rotation-alignments: the azimuthal position of the Sun and all sky-positions was taken in reference to the measured data. The highest value for each set of calibrated incident illuminance data represented the Sun position, which was identified by running a script to list the azimuthal and altitudinal indices of the highest data-point in each batch, as demonstrated in Figure 6a. The sun-position used for this work was the one assessed from the patch of highest incident illuminance. This was done to minimise the errors in device re-orientation; the primary angle of interest (χ) depends on the difference between sun-position to a patch's position and is irrespective of the device's true azimuthal orientation. This approach however might not work for overcast days, and with better azimuthal control in the device, the theoretical sun-path could be used in future developments.

The measured data was converted to sky-maps to assess the sun-path; while the sun-path was continuous through the sky-maps, the position of Sun was at times measured in two or three consecutive patches as demonstrated in Figure 7(b). This was due to low scan efficiency arising from rigidly defined patch locations, with partial overlaps affecting measurements for the circumsolar regions. These sets defined the transition phase between patches where high illuminance was logged at non-singular positions. The python script selected the first appearing location index with the highest illuminance value for each set, which thus deviated in its indices as compared to theoretically continuous sun-path as demonstrated in Figure 7. In such cases, a jump was seen in the apparent sun position for consecutive time-points as demonstrated in the green rectangle in Figure 7(a).

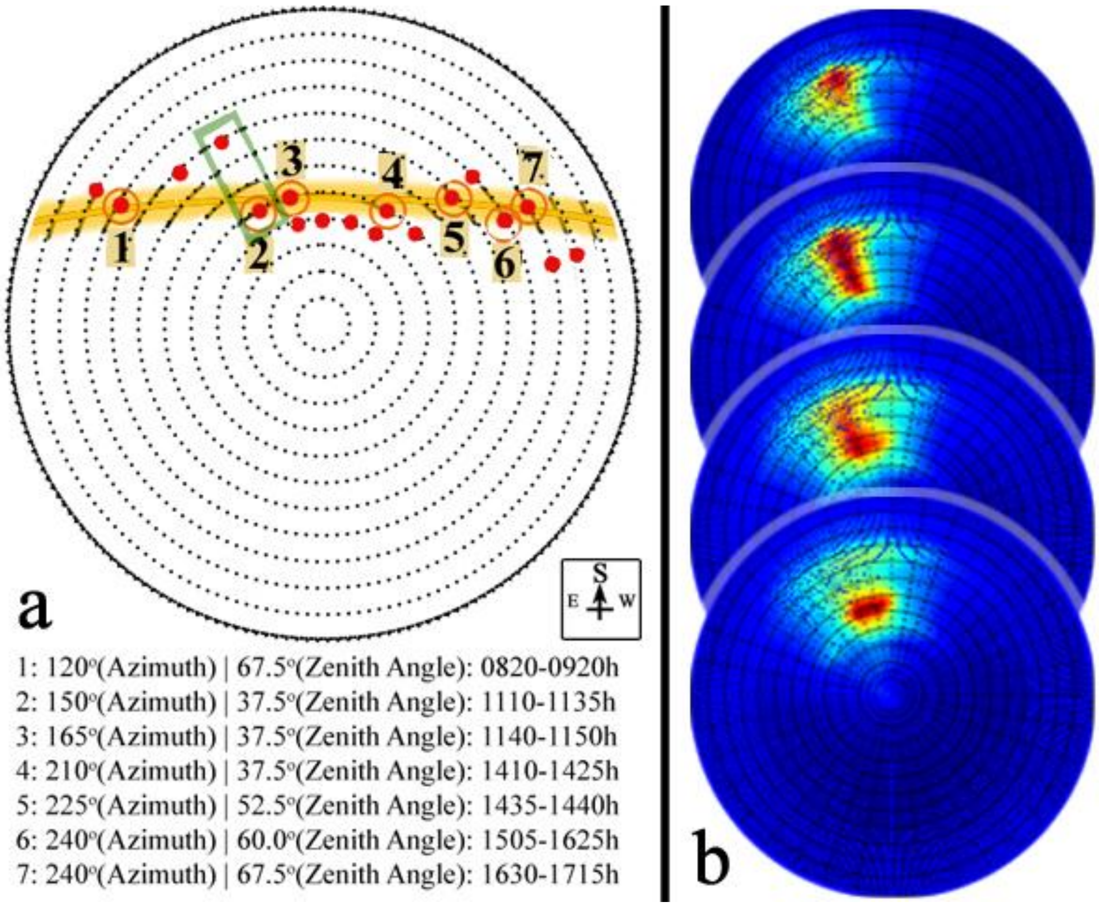

Figure 7: a) Theoretical sun-trajectory (yellow) with assessed sun position for various batches through the day (red). The positions of interest marked with red circle and described underneath. b) Transition zone between patches as measured: high incident illuminance measured at non-singular positions

5.2 Modelled virtual sky-dome datasets

To compare with the measured incident angular illuminance datasets individually and identify the closest sky-model, the virtual sky-dome datasets for all time-points were calculated for each 15 CIE sky-types. The coefficients were taken from the tabulated values, and the dynamic sun-position and each patch's defined position provided the necessary angular values. For each sky-patch, the altitude angle (α) is rigidly pre-defined, and after identifying sun position for each time point as described in Section 5.1, the sun-distance (χ) for each 265 sky-patches was dynamically calculated using Equation 2. With the respective coefficients as tabulated in Table 1, along with equations 1 through 6, the modelled sky-distribution datasets were generated for each time-point for all 15 CIE sky-types. These modelled virtual sky-domes represent normalized sky-luminance values, for all sky-positions with respect to zenith: the zenith luminance remains 1 — and the luminance of all other sky-positions is a ratio of zenith luminance, as demonstrated in Figure 8.

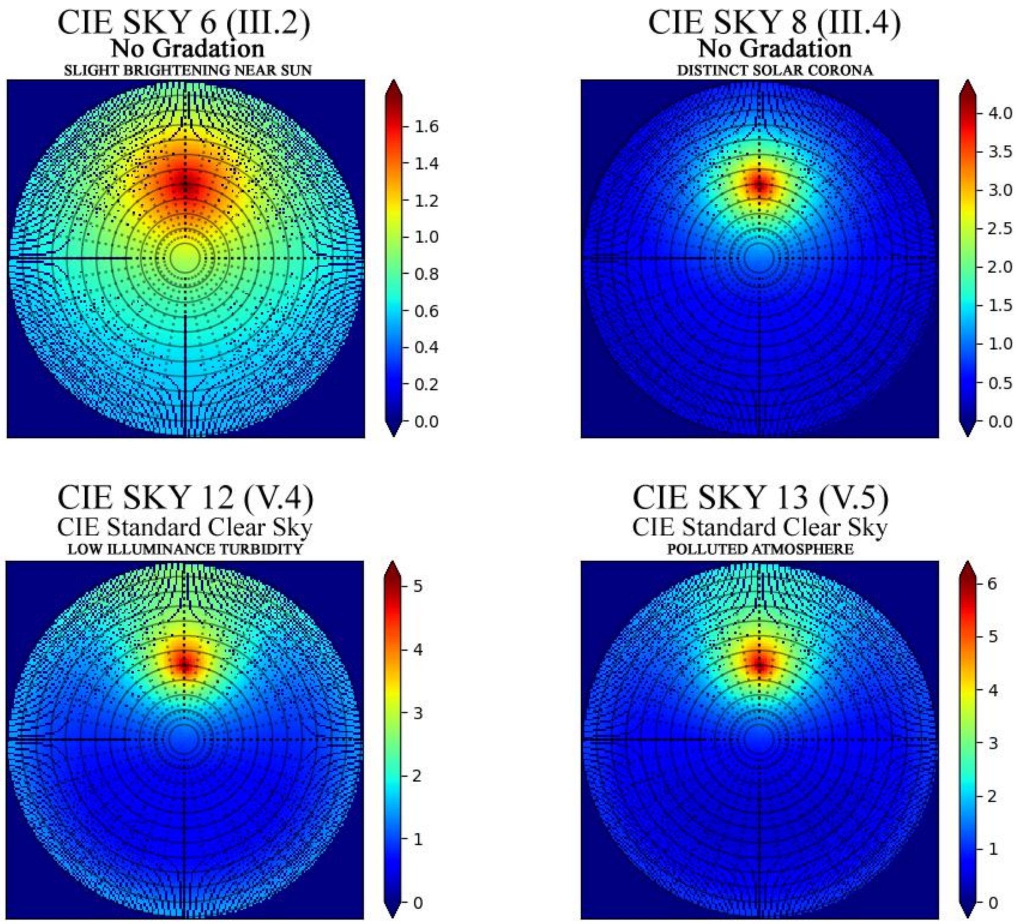

Figure 8: Modelled Virtual Sky-domes for few CIE skies based on Sun position (12:30h on 30 Jan 2018)

5.3 RMSD based assessment of closest CIE sky

Each measured dataset was normalized using its zenith luminance: a script was used for batch conversion of all datasets, dividing incident illuminance for all 288 positions with the average incident illuminance at zenith for each time-point. This generated normalized measured dataset for various time-points with an interval of 5-minutes.

For each dataset, comparison was drawn between the measured normalized incident illuminance for each sky-position with the modelled values for each sky. In total, the 265 luminance values for each of the 540 sets were compared with 265x15 skies for each set. To identify the closest sky for any set (representative of the time-point), the Root Mean Square Deviation (RMSD) was used. The RMSD is calculated as:

$$\mathrm{RMSD} = \sqrt{\frac{\sum_{1}^{265}(\mathrm{Lux}_{\mathrm{measured}} - \mathrm{Lux}_{\mathrm{sky\ model}})^2}{265}} \quad (7)$$

Here $\mathrm{Lux}_{\mathrm{measured}}$ and $\mathrm{Lux}_{\mathrm{sky\ model}}$ are the normalized luminance values for measured and modelled dataset for all 15 CIE skies, and 265 represents the number of discrete sky-positions in each set. The CIE sky set with minimum RMSD as compared to measured sky was chosen as the closest CIE sky for each set.

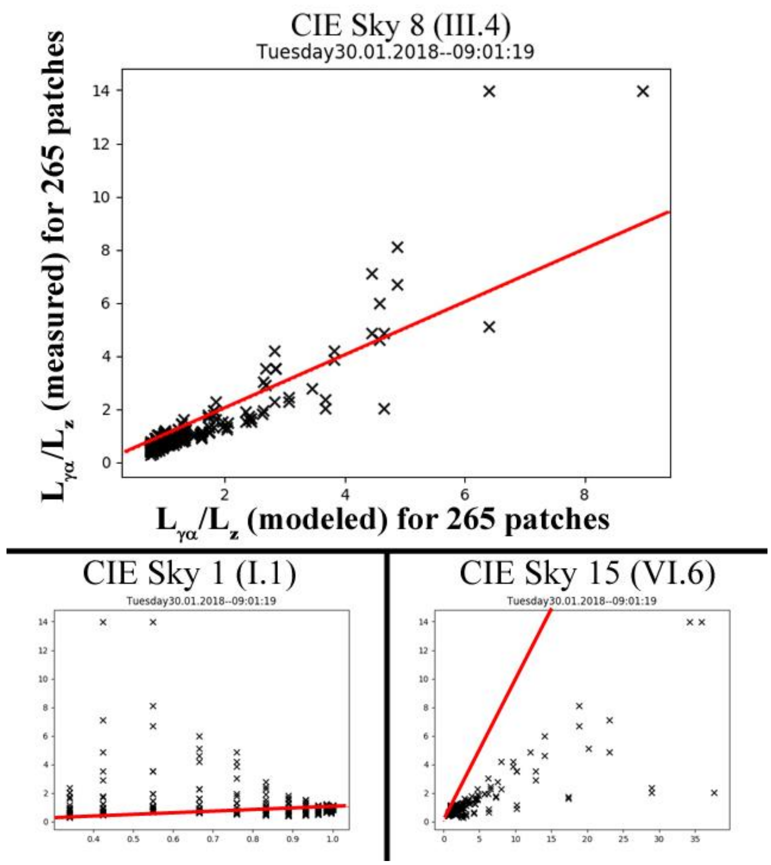

Figure 9: Plotting modeled and measured sky-luminance for various CIE skies at a specific time-point, Red line indicates a pre-defined slope of unity, with a good match expecting scatter around the slope.

In a graphical representation, the two axes represent the measured (normalized) and modeled values for all sky-positions, as demonstrated in Figure 9. A slope 1 line was plotted in red, and proximity of the scatter to slope-1 line was expected for a good fit of the measured dataset to either model-sky. For the same time-point (0901h on 30 Jan 2018), CIE sky 8 is seen as better match, as compared to Sky 1 and Sky 15, as demonstrated in Figure 9. Figure 10 demonstrates the comparison for time-points set with an interval of 2 hours through a test day. The selected skies with minimum RMSD are highlighted, and Table 4 presents the RMSD values for the scatters demonstrated in Figure 10.

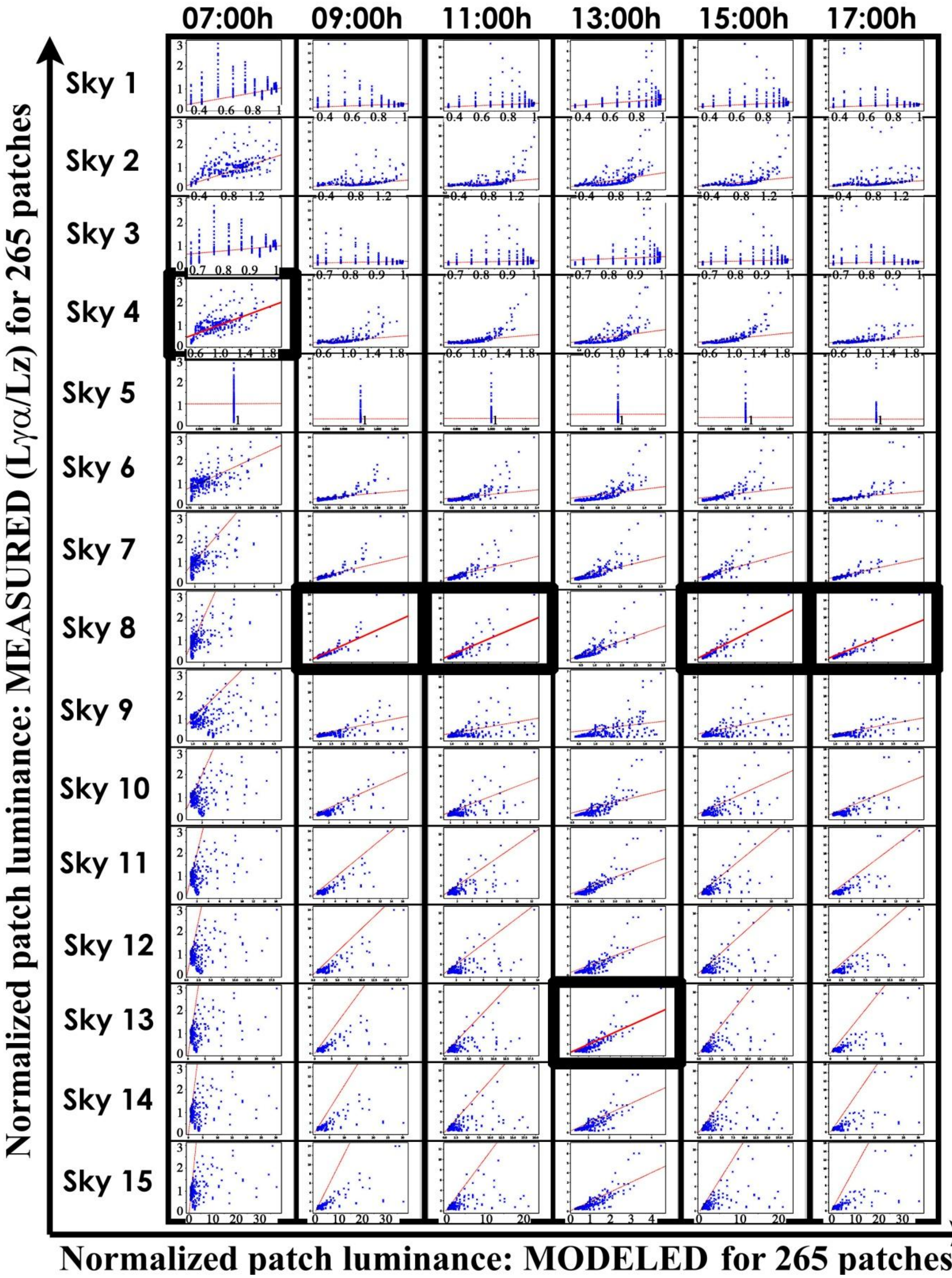

Figure 10: Comparing measured and modelled normalized patch luminance (Lγα/Lz) for all 265 sky positions through two-hour interval during the day (30 Jan 2018). Horizontal axis defines the modelled data for each patch, whereas the measured data for the same patch is plotted in vertical axis. A good fit is expected for scatter around the red line (defined as slope 1 line everywhere)

In the CIE sky-model, sky-types 1, 3 and 5 are azimuthally independent (overcast sky-types with no role of sun position). As such, the quantization along horizontal axis in sky-types 1 and 3 show the variation in 24 measured data points for uniform modeled data along 24 azimuthal positions: the modeled data remaining constant for all azimuthal locations at that altitudinal position. Sky 5 is a total overcast sky-type; with illuminance at all sky-positions being the same as that at zenith, and thus the graphs show 265 measured values across fixed modeled value. These sky-types are for representation and the closest sky-type for Mumbai during the day were not overcast sky (rare instance near dusk period after the sun-down).

Table 4: RMSD between measured and modelled luminance distribution data for 265 patches

	Time of Day (30 Jan 2018, Mumbai)					
Sky Type	**7:00**	**9:00**	**11:00**	**13:00**	**15:00**	**17:00**
1	0.500162	1.606877	1.374295	0.822901	1.336197	1.831773
2	0.407801	1.469672	1.211835	0.717796	1.175091	1.708449
3	0.438488	1.550427	1.350444	0.839578	1.313088	1.782663
4	**0.325985**	1.363335	1.161186	0.703804	1.124053	1.613859
5	0.420423	1.50262	1.340882	0.886237	1.304756	1.741377
6	0.328794	1.263036	1.124564	0.702441	1.087601	1.525407
7	0.511806	0.997878	0.915039	0.592465	0.886475	1.292865
8	0.900232	**0.727035**	**0.737236**	0.510356	**0.730186**	**1.061323**
9	0.863931	1.140506	1.236112	0.830277	1.207294	1.408111
10	1.336433	0.98264	1.183803	0.647276	1.169959	1.235714
11	2.05827	1.249897	1.361098	0.514938	1.368338	1.398931
12	2.661199	1.848033	1.806649	0.579704	1.815701	1.930641
13	3.547235	2.604063	2.237177	**0.490348**	2.253843	2.623282
14	4.560418	3.678176	2.953163	0.580407	2.969188	3.674757
15	5.651898	4.727835	3.455699	0.511399	3.471792	4.699266

The sky-type varies dynamically based on ambient conditions, and the RMSD based sky-type recommendation approach is extended towards identifying the diurnal sky-variation. The closest sky-type for each reading taken every 5-minute on the test days was tabulated through the hours. Figure 11 demonstrates the occurrence of closest CIE skies with time on the representative days. It was observed that the sky distribution followed an overcast-intermediate-clear curve in the morning hours and the opposite in the evening hours.

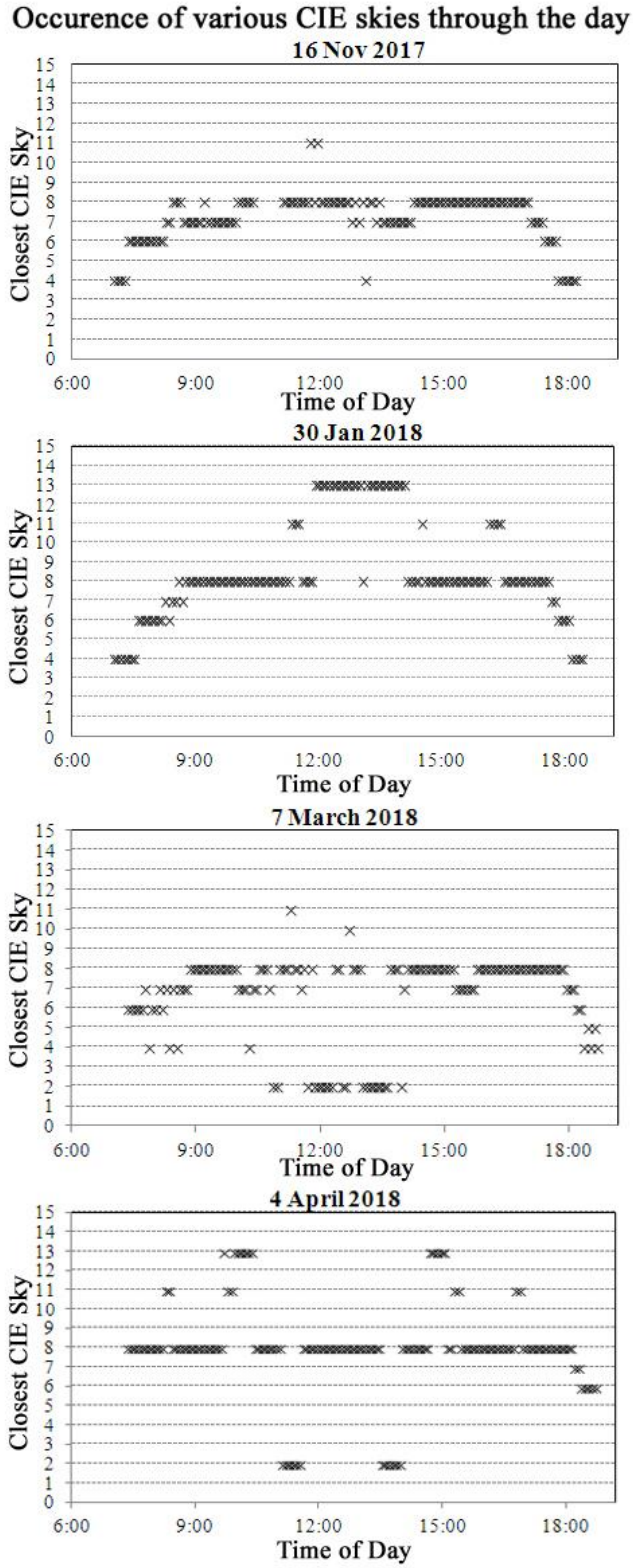

Figure 11: Occurrence of closest CIE skies through various hours of the representative days

The frequency of occurrence for different skies through the test-period is demonstrated in Figure 12. Sky type 8 is seen dominating the test period, with types 4, 6, and 7 seen prominently (Sky 8 governing over 50% of the daytime for all test cases (51.6% in November, 53.6% in January, 52.6% in March and 71.5% in April).

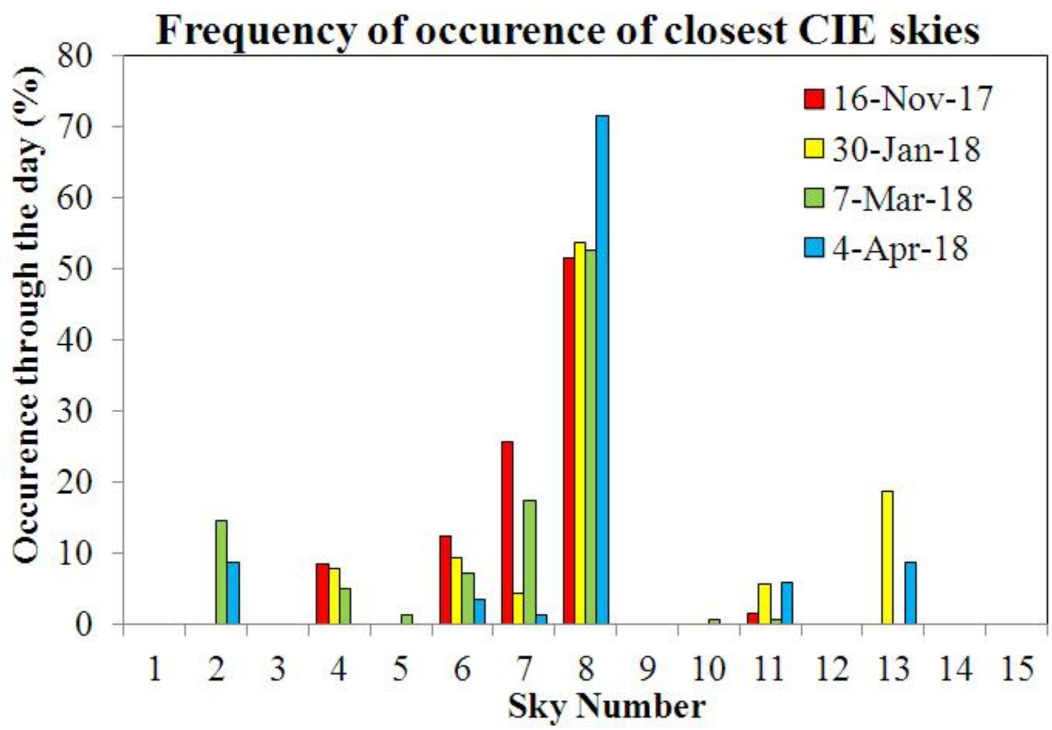

Figure 12: Frequency of occurrence of various CIE skies over the test days

5.5 Comparing closest CIE sky with measured data

Another approach to identify sky-type was done through analyzing the luminance-distribution curves. Most sky-types identified through measurements taken from our device — Sky-types 6, 7 and 8 — are models with no gradation. As such, the primary factor affecting incident illuminance distribution for a patch is the sun-distance (χ) of a certain patch. Thus, a comparison of measured normalized incident illuminance scatter with sun-distance was conducted with characteristic scatter curves obtained for model skies.

After determining solar position (altitude/azimuth) for each batch, a python script generated the sun-distance (χ) for each of the 288 data-points of each set, corresponding to 265 sky-positions. The incident illuminance data from each patch was normalized with the incident illuminance from zenith for each set, to generate the normalized values for each patch for each set. Figure 13 demonstrates a distribution of normalized patch measurements for various positions at different angular distances from the Sun, at various times in the day. Also, a superimposition of all sets through the day is demonstrated. A comparison of the obtained distribution with the characteristic curves for all sky-models (for the defined solar-position) can also be used to identify closest sky-model for a dataset.

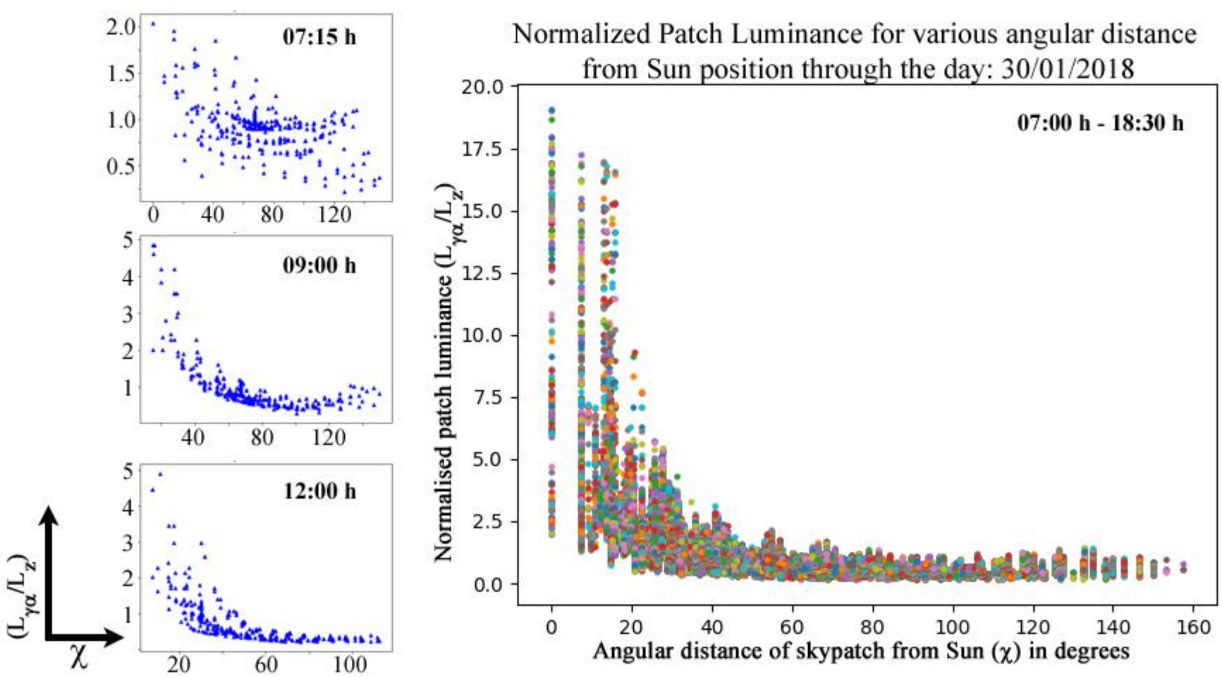

Figure 13: Normalized incident patch illuminance for various positions at distance χ from the sun at different times through the day, and a superimposition of all distributions for the day (30 Jan 2018)

Figure 14 demonstrates the comparison between measured normalized luminance and corresponding closest sky luminance distribution in terms of sky maps. Also, a comparison between luminance distribution at various sun-distance angles is demonstrated with characteristic curves for closest sky-models.

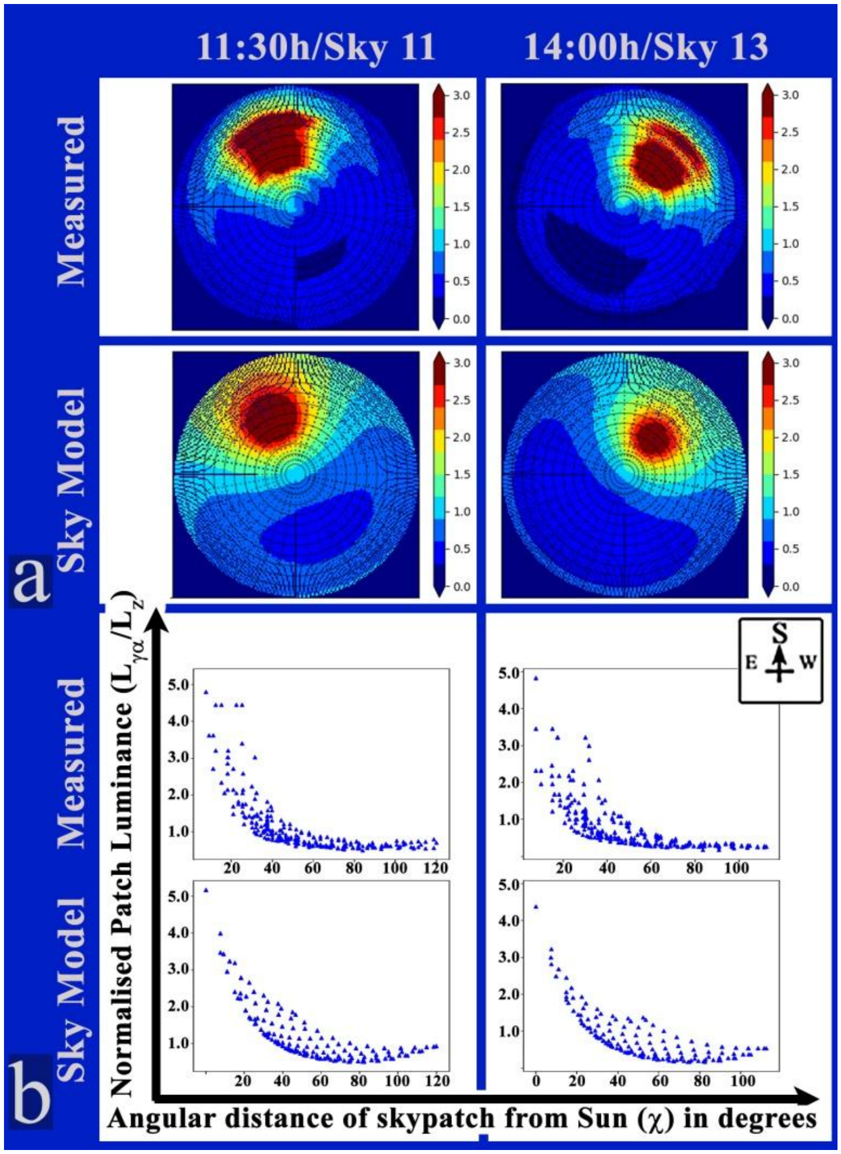

Figure 14: Comparison between measured and modelled closest skies for various hours as: a) Sky maps, b) Luminance distribution scatter with angular distance from Sun

6. Discussion

Existing building simulation packages are advanced, and perform whole building energy analysis. However, there is a scope of improvement: while most input parameters such as weather data and buildings' operations are relatively easy to measure and define, the realistic indoor illuminance prediction may be discerned as a research gap. Indoor illuminance is dependent on angular sky-luminance distribution — which is dynamic. The CIE sky-models can predict the sky-luminance distribution in absence of measurement equipments, but there is a need of identifying which sky-type to input as the appropriate model for a given instance at a location. The simulation packages favor generic sky-models — CIE standard overcast sky model, and the CIE standard clear sky model — to compute indoor illuminance distribution (pathway 1 of Figure 1). The predicted indoor illuminance may be highly offset from their realistic values in absence of the appropriate model. Devices may be used to measure angular sky-luminance distribution and provide realistic luminance data/incident illuminance measurements of the dynamic sky for calculating the indoor illuminance. However, creating entirely new simulation packages for predicting indoor illuminance based on measured luminance distribution data-sets (pathway 3 of Figure 1) provides challenges to come on-par with existing packages in terms of other calculations: thermal, mechanical, etc in building energy analysis.

In this paper, we have discussed an intermediate solution (pathway 2 of Figure 1) — a protocol for identifying the closest CIE model for a given time-point, through statistical analysis and qualitative assessment. The curves of normalized sky-luminance at a patch ($L_{\gamma\alpha}/L_z$) with respect to the sun-distance (χ) for all patches may be compared with characteristic curves for all 15 sky-models to qualitatively identify the closest CIE sky-model at that time-point. The RMSD based assessment between measured and modelled normalized luminance for all 265 patches can be used to quantitatively identify the closest CIE sky-model for a time-point.

This approach provides a possibility of enhancing existing open source building simulation packages through creating custom scripts. This way, similar to weather data input for fixed time-instances, an identifier for closest CIE sky for each hour may be defined for calculating the ambient sky luminance distribution, without having to input the large measured data-sets. There is also a possibility of extending this work using a Fuzzy Logic approach. In the present form, the sky-types are rigidly defined using CIE's most probable skies, but the fuzzy-logic approach could be used to counter the 'threshold effect' for closest sky-types for consecutive time-points. This way, the range in sky-clarity could be enhanced towards a more continuous form, and the measured data could be reduced towards a smoother transition in sky-clarity.

7. Conclusions

We present the comparative analysis of measured incident sky illuminance data with 15 CIE sky-models at Mumbai to establish the closest sky at various times through the day. Incident illuminance data from spatially-discretized sky positions measured at Mumbai with a novel LDR based device design over four representative days selected across five-month period was analyzed and compared with model skies. For the representative data spanning 540 data-sets over 5 minute intervals, a range of 9 different sky-types was seen based on the minimum root mean squared deviation method. Sky type 8 (CIE III.4) was seen dominating over 50% of the daytime for all four representative days. Hourly analysis demonstrated a trend from overcast-intermediate-clear sky during early hours and opposite during later hours of the day.

The approach of measurement based modelling — reducing the measured sky-luminance distribution into closest sky-model indicator — has the advantage of simplifying the input for existing building simulation programs. Based on solar position and input sky-type, the modelled sky-distribution dataset can be generated in the simulation packages for further calculation of indoor illuminance. This way, the user can feed an indicator for the closest sky-type, eliminating the need for incorporating the bulk of measured incident angular illuminance distribution arrays for each time-point. The indoor illuminance measurement predictions and the overall building performance analysis can thus be more realistic, as compared to those calculated using generic models at all time-points.

Acknowledgement

The first author is grateful to Dr. Ronita Bardhan, Dr. Suneet Singh and Dr. Neelam Rathore for their constructive suggestions and discussions.

Funding Sources and additional information

This research did not receive any specific grant from funding agencies in the public, commercial, or not-for-profit sectors.

References

[1] X. Cao, X. Dai, J. Liu, Building energy-consumption status worldwide and the state-of-the-art technologies for zero-energy buildings during the past decade, Energy Build. 128 (2016) 198–213. doi:10.1016/J.ENBUILD.2016.06.089.

[2] A.K. Jain, A Report on Energy Efficiency and Energy Mix in the Indian Energy System (2030), 2015. https://www.gita.org.in/Attachments/Reports/Energy_Efficiency.pdf (accessed August 10, 2017).

[3] M. Zinzi, A. Mangione, The daylighting contribution in the electric lighting energy uses: EN standard and alternative method comparison, in: Energy Procedia, 2015: pp. 2663–2668. doi:10.1016/j.egypro.2015.11.342.

[4] S.K.H. Chow, D.H.W. Li, E.W.M. Lee, J.C. Lam, Analysis and prediction of daylighting and energy performance in atrium spaces using daylight-linked lighting controls, Appl. Energy. 112 (2013) 1016–1024. doi:10.1016/j.apenergy.2012.12.033.

[5] S. Sankhe, I. Vittal, R. Dobbs, A. Mohan, A. Gulati, J. Ablett, S. Gupta, A. Kim, S. Paul, A. Sanghvi, G. Sethy, McKinsey, India's urban awakening : Building inclusive cities , sustaining economic growth, McKinsey Q. (2010) 207.

[6] B.P. Jelle, Solar radiation glazing factors for window panes, glass structures and electrochromic windows in buildings - Measurement and calculation, Sol. Energy Mater. Sol. Cells. 116 (2013) 291–323. doi:10.1016/j.solmat.2013.04.032.

[7] Adrian Tuluca, Energy efficient design and construction for commercial buildings, McGraw Hill, New York, 1997.

[8] M. Košir, N. Iglič, R. Kunič, Optimisation of heating, cooling and lighting energy performance of modular buildings in respect to location's climatic specifics, Renew. Energy. 129 (2018) 527–539. doi:10.1016/j.renene.2018.06.026.

[9] G. Zrim, M. Mihelčič, L.S. Perše, B. Orel, B. Simončič, R. Kunič, Light distribution in air-supported pneumatic structures: Comparison of experimental and computer calculated

daylight factors, Build. Environ. 119 (2017) 110–127. doi:10.1016/j.buildenv.2017.04.005.
[10] J.C. Xie, P. Xue, C.M. Mak, J.P. Liu, Balancing energy and daylighting performances for envelope design: A new index and proposition of a case study in Hong Kong, Appl. Energy. 205 (2017) 13–22. doi:10.1016/j.apenergy.2017.07.115.
[11] K.K. Chong, N.O. Onubogu, T.K. Yew, C.W. Wong, W.C. Tan, Design and construction of active daylighting system using two-stage non-imaging solar concentrator, Appl. Energy. 207 (2017) 45–60. doi:10.1016/j.apenergy.2017.05.188.
[12] M.S. Mayhoub, D.J. Carter, The costs and benefits of using daylight guidance to light office buildings, Build. Environ. 46 (2011) 698–710. doi:10.1016/j.buildenv.2010.09.014.
[13] E.J. Gago, T. Muneer, M. Knez, H. Köster, Natural light controls and guides in buildings. Energy saving for electrical lighting, reduction of cooling load, Renew. Sustain. Energy Rev. 41 (2015) 1–13. doi:10.1016/j.rser.2014.08.002.
[14] A.A. Elmualim, S. Smith, S.B. Riffat, L. Shao, Evaluation of dichroic material for enhancing light pipe/natural ventilation and daylighting in an integrated system, Appl. Energy. 62 (1999) 253–266. doi:10.1016/S0306-2619(99)00014-8.
[15] D.H.W. Li, A review of daylight illuminance determinations and energy implications, Appl. Energy. 87 (2010) 2109–2118. doi:10.1016/j.apenergy.2010.03.004.
[16] A. Karkare, A. Dhariwal, S. Puradbhat, M. Jain, Evaluating Retrofit Strategies for Greening Existing Buildings by Energy Modelling & Data Analytics, in: Int. Conf. Intell. Green Build. Smart Grid, Taipei, 2014: pp. 1–4.
[17] V. Bazjanac, T. Maile, C. Rose, T.O.D. James, An assessment of the use of building energy performance simulation in early design, Proc. 12th …. (2011) 14–16. http://www.ibpsa.org/proceedings/BS2011/P_1531.pdf.
[18] A. Brun, C. Spitz, E. Wurtz, L. Mora, Behavioural Comparison of Some Predictive Tools Used in a Low-Energy Building, Elev. Int. IBPSA Conf. (2009) 1185–1190.
[19] K. Kensek, J. Suk, Daylight Factor (overcast sky) versus Daylight Availability (clear sky) in Computer-based Daylighting Simulations, J. Creat. Sustain. Archit. Built …. 1 (2011) 3–14. http://www.sersc.org/journals/CSABE/vol1/2.pdf.
[20] S.G. Attia, A. De Herde, Early design simulation tools for net zero energy buildings: A comparison of ten tools, Proc. Build. Simul. 2011 12th Conf. Int. Build. Perform. Simul. Assoc. (2011) 94–101. http://www.scopus.com/inward/record.url?eid=2-s2.0-84870207999&partnerID=tZOtx3y1.
[21] I. Acosta, C. Varela, J.F. Molina, J. Navarro, J.J. Sendra, Energy efficiency and lighting design in courtyards and atriums: A predictive method for daylight factors, Appl. Energy. 211 (2018) 1216–1228. doi:10.1016/j.apenergy.2017.11.104.
[22] G.N. Tiwari, A. Tiwari, Shyam, Handbook of Solar Energy : Theory, Analysis and Applications, Springer Nature, Singapore, 2016.
[23] P. Moon, D. Spencer, Illumination from a non-uniform sky, Trans Illum Eng Soc. 37 (1942) 707–726.
[24] S. Darula, R. Kittler, CIE General sky standard defining luminance distributions, ESim. (2002) 8.
[25] R. Kittler, M. Kocifaj, S. Darula, Daylight Science and Daylight Technology, Springer, New York, 2012.
[26] D.H.W. Li, C.C.S. Lau, J.C. Lam, A Study of 15 Sky Luminance Patterns against Hong Kong Data, Archit. Sci. Rev. 46 (2003) 61–68. doi:10.1080/00038628.2003.9696965.

[27] V. Ferraro, V. Marinelli, M. Mele, A method for selecting the CIE standard general sky model with regard to calculating luminance distributions, J. Atmos. Solar-Terrestrial Phys. 95–96 (2013) 59–64. doi:10.1016/j.jastp.2013.01.006.
[28] V. Mettanant, P. Chaiwiwatworakul, S. Chirarattananon, A model of Thai's sky luminance distribution based on reduced CIE standard sky types, Renew. Energy. 103 (2017) 739–749. doi:10.1016/j.renene.2016.11.008.
[29] T. Luo, D. Yan, R. Lin, J. Zhao, Sky-luminance distribution in Beijing, Light. Res. Technol. 47 (2015) 349–359. doi:10.1177/1477153514532466.
[30] S.K. Wittkopf, L.K. Soon, Analysing sky luminance scans and predicting frequent sky patterns in Singapore, Light. Res. Technol. 39 (2007) 31–51. doi:10.1177/1365782806070683.
[31] K.A. Alshaibani, Classification Standard Skies: The use of horizontal sky illuminance, Renew. Sustain. Energy Rev. 73 (2017) 387–392. doi:10.1016/j.rser.2017.01.116.
[32] D.H.W. Li, C.C.S. Lau, J.C. Lam, Overcast sky conditions and luminance distribution in Hong Kong, Build. Environ. 39 (2004) 101–108. doi:10.1016/j.buildenv.2003.06.001.
[33] Autodesk Help, CIE Sky Model | 3ds Max | Autodesk Knowledge Network, (2017). https://knowledge.autodesk.com/support/3ds-max/learn-explore/caas/CloudHelp/cloudhelp/2017/ENU/3DSMax/files/GUID-3636C39D-DAC5-4329-932F-196FDD61AB30-htm.html (accessed April 29, 2018).
[34] Designbuilder, Daylighting Calculation Options, (2015). https://www.designbuilder.co.uk/helpv3.4/Content/Daylighting_Calculation_Options.htm (accessed June 12, 2018).
[35] M. Inanici, A. Hashemloo, An investigation of the daylighting simulation techniques and sky modeling practices for occupant centric evaluations, Build. Environ. 113 (2017) 220–231. doi:10.1016/j.buildenv.2016.09.022.
[36] L. Komar, A. Rusnak, R. Dubnicka, Analysis of diffuse irradiance from two parts of sky vault divided by solar meridian using portable spectral sky-scanner, Sol. Energy. 96 (2013) 1–9. doi:10.1016/j.solener.2013.07.003.
[37] J.T. Kider, D. Knowlton, J. Newlin, Y.K. Li, D.P. Greenberg, A framework for the experimental comparison of solar and skydome illumination, ACM Trans. Graph. 33 (2014) 1–12. doi:10.1145/2661229.2661259.
[38] F.J. Casares, J. Ramírez-Faz, R. López-Luque, Development of synthetic hemispheric projections suitable for assessing the sky view factor on horizontal planes, Energy Build. 82 (2014) 696–702. doi:10.1016/j.renene.2014.08.025.
[39] A.N.M. Shahriar, Exploration into sky brightness capture through digital camera configuration, in: 44th Annu. Conf. Archit. Sci. Assoc. ANZAScA 2010, 2010.
[40] M. Maskarenj, R. Banerjee, P.C. Ghosh, Design and development of a low-cost angular sky luminance measurement system, Build. Environ. 142 (2018) 22–33. doi:10.1016/j.buildenv.2018.06.001.
[41] BigLadder, EnergyPlus weather data dictionary, (2015). http://bigladdersoftware.com/epx/docs/8-3/auxiliary-programs/energyplus-weather-file-epw-data-dictionary.html (accessed November 12, 2016).
[42] R. Guglielmetti, D. Macumber, N. Long, OpenStudio: An Open Source Integrated Analysis Platform, Build. Simul. 2011 12th Conf. Int. Build. Perform. Simul. Assoc. (2011) 442–449. http://www.osti.gov/bridge.
[43] J. Hu, S. Olbina, An expert system based on openstudio platform for evaluation of

daylighting system design, Comput. Civ. Eng. - Proc. 2013 ASCE Int. Work. Comput. Civ. Eng. (2013) 186–193. doi:10.1061/9780784413029.024.
[44] H. Wang, Z. (John) Zhai, Advances in building simulation and computational techniques: A review between 1987 and 2014, Energy Build. 128 (2016) 319–335. doi:10.1016/j.enbuild.2016.06.080.
[45] A. Suárez-García, D. Granados-López, D. González-Peña, M. Díez-Mediavilla, C. Alonso-Tristán, Seasonal caracterization of CIE standard sky types above Burgos, northwestern Spain, Sol. Energy. 169 (2018) 24–33. doi:10.1016/j.solener.2018.04.028.
[46] Comission Internationale de L'Eclairage, Spatial distribution of daylight-CIE standard general sky, 2003.
[47] F. Ciampini, P.S. Scarazzato, A.A.R. Neves, D.C.L. Pereira, M.H. Yamanaka, Low cost data acquisition module for evaluating the quantitative performance of daylight systems, Sol. Energy. 81 (2007) 1187–1190. doi:10.1016/j.solener.2007.01.013.
[48] P.R. Tregenza, Subdivision of the sky hemisphere for luminance measurements, Light. Res. Technol. 19 (1987) 13–14. doi:10.1177/096032718701900103.
[49] M. Maskarenj, G. Chawla, R. Banerjee, P.C. Ghosh, Light Dependent Resistor based angular Daylight distribution measurement device, Feb 28. Indian Patent App. 201821007607, 2018.
[50] M. Kottek, J. Grieser, C. Beck, B. Rudolf, F. Rubel, World map of the Köppen-Geiger climate classification updated, Meteorol. Zeitschrift. 15 (2006) 259–263. doi:10.1127/0941-2948/2006/0130.
[51] S.P. Sukhatme, J.K. Nayak, Solar energy : principles of thermal collection and storage, Tata McGraw-Hill, 2008. https://books.google.co.in/books/about/Solar_Energy.html?id=O8IMS-jq6skC (accessed May 5, 2018).